

Article

g-C₃N₄-Stabilised Organic–Inorganic Halide Perovskites for Efficient Photocatalytic Selective Oxidation of Benzyl Alcohol

Menglong Zhang, Weizhe Wang, Fangliang Gao *  and Dongxiang Luo *

Institute of Semiconductors, South China Normal University, Guangzhou 510631, China; mlzhang@m.scnu.edu.cn (M.Z.); weizhewang@m.scnu.edu.cn (W.W.)

* Correspondence: gaofl@m.scnu.edu.cn (F.G.); luodx@gdut.edu.cn (D.L.)

Abstract: The outstanding optoelectronic performance and facile synthetic approach of metal halide perovskites has inspired additional applications well beyond efficient solar cells and light emitting diodes (LEDs). Herein, we present an alternative option available for the optimisation of selective and efficient oxidation of benzylic alcohols through photocatalysis. The materials engineering of hybrids based on formamidinium lead bromide (FAPbBr₃) and graphitic carbon nitride (g-C₃N₄) is achieved via facile anti-solvent approach. The photocatalytic performance of the hybrids is highly reliant on weight ratio between FAPbBr₃ and g-C₃N₄. Besides, the presence of g-C₃N₄ dramatically enhances the long-term stability of the hybrids, compared to metal oxides hybrids. Detailed optical, electrical and thermal studies reveal the proposed novel photocatalytic and stability behaviours arising in FAPbBr₃ and g-C₃N₄ hybrid materials.

Keywords: perovskites; carbon nitride; photocatalysis

Citation: Zhang, M.; Wang, W.; Gao, F.; Luo, D. g-C₃N₄-Stabilised Organic–Inorganic Halide Perovskites for Efficient Photocatalytic Selective Oxidation of Benzyl Alcohol. *Catalysts* **2021**, *11*, 505. <https://doi.org/10.3390/catal11040505>

Academic Editors: Víctor A. de la Peña O'Shea, Gerardo Colón Ibañez and Fernando Fresno

Received: 24 March 2021
Accepted: 13 April 2021
Published: 16 April 2021

Publisher's Note: MDPI stays neutral with regard to jurisdictional claims in published maps and institutional affiliations.



Copyright: © 2021 by the authors. Licensee MDPI, Basel, Switzerland. This article is an open access article distributed under the terms and conditions of the Creative Commons Attribution (CC BY) license (<https://creativecommons.org/licenses/by/4.0/>).

1. Introduction

As a promising family of semiconductor materials, organic–inorganic halide perovskites (OIHPs) have attracted massive attentions attributing to their potential applications in optoelectronic field. This can be summarised as several advantages of OIHPs over other typical semiconductor materials, including tunable band gap energy, low-cost and facile synthesising [1]. In addition, thanks to the superior light harvesting efficiency of OIHPs [2] halide perovskites-based solar cells have performed high solar energy conversion efficiency approached 25.2% (NERL, Best Research-Cell Efficiency Chart). While OIHPs-based conversion of solar energy continues to embody mainstream halide perovskites research, the potential applications toward photochemical processes remains rarely explored. The main issues are the poor stability of OIHPs, which would decompose and cause Pd leaking, especially in presence of polar solvent.

In addition to the perovskite, after it was triggered by the seminal work by Wang et al. [3] graphite carbon nitride (g-C₃N₄) is at present a prominent photoactive material within fundamental research among many candidates, because of the tunable band gap energy (by designing N-rich or C-rich C₃N₄) [4,5], stability under harsh chemical conditions [6] and metal-free. The high stability and poor solubility of g-C₃N₄ in general solvents allow its utilisations as an effective heterogeneous catalyst [7], particularly as photocatalyst for solar to chemical bond conversions, such as oxygen generation [8,9], hydrogen evolution [4,5,10] and overall water splitting [11]. On the other hand, OIHPs indicate potential capabilities to extend highly efficient light harvesting in visible wavelength region. While in aqueous systems, the instability nature of OIHPs generally limits their utilisations in typical photocatalytic processes including water splitting, CO₂ reduction and degradation of organic pollutants. These limitations were commonly solved by using an oversaturated aqueous HX solution (X is depending on the halide ion in OIHPs) as sacrificial reagent, thus extended their applications to reduction of CO₂ and oxidation of PEDOT [12]. A typical type-II band structure could be formed by FAPbBr₃/C₃N₄, and it is

expected to give an enhanced charge separation [13]. In addition, it was reported that the amine group ($-\text{NH}_2$) of $g\text{-C}_3\text{N}_4$ could effectively bind to the surface and expose the steric hindrance $-\text{OH}$ groups to prevent typical polar solvent including ethanol, methanol or isopropanol [14], thus optimising the stability of OIHPs. Furthermore, during the preparation of samples, it is unavoidable that the pristine $g\text{-C}_3\text{N}_4$ and OIHPs would be in presence in the as-prepared $\text{FAPbBr}_3/\text{C}_3\text{N}_4$ hybrids, therefore the possible influence of pristine $g\text{-C}_3\text{N}_4$ on hybrids should also be considered due to its higher oxidation potential than FAPbBr_3 . Based on these highly interesting properties of $g\text{-C}_3\text{N}_4$ and OIHPs, constructing the $\text{FAPbBr}_3/\text{C}_3\text{N}_4$ hybrids offers a path to exploit efficient selective and stable oxidation of alcohols to carbonyls, which is an important industrial organic reaction [15].

Herein we report the photocatalyst based on $\text{FAPbBr}_3/\text{C}_3\text{N}_4$ for efficient and selective photoactivated oxidation of benzylic alcohol. Through utilisation of the band alignment of photogenerated electrons/holes in $\text{FAPbBr}_3/\text{C}_3\text{N}_4$ hybrids, and modification of ratios between the two materials, the optimised photocatalytic performance under visible light is achieved. Besides, the photostability behaviour, optical, photochemical and thermal properties of $\text{FAPbBr}_3/\text{C}_3\text{N}_4$ hybrids are demonstrated with details.

2. Result and Discussion

2.1. Structure and Morphologies

The FAPbBr_3 and $\text{FAPbBr}_3/\text{C}_3\text{N}_4$ samples are prepared using a modified facile anti-solvent precipitation method [16], with detailed procedure provided in the Supporting Information. Pristine $g\text{-C}_3\text{N}_4$ (JCPDS 87-1526) and FAPbBr_3 (congruent with the previous report [17]) crystallise into their most thermodynamically stable graphite and cubic phase, respectively (Figure S1, Powder X-ray diffraction (PXRD)). The diffraction patterns of $\text{FAPbBr}_3/\text{C}_3\text{N}_4$ are consistent with both phases, suggesting a successful synthesis of $\text{FAPbBr}_3/\text{C}_3\text{N}_4$ hybrid. In the next, the morphologies of $g\text{-C}_3\text{N}_4$, FAPbBr_3 and $\text{FAPbBr}_3/\text{C}_3\text{N}_4$ samples prepared using modified anti-solvent method are confirmed by scanning electron microscopy (SEM), as it is shown in Figure S2a, the average size of FAPbBr_3 synthesised from pure precursor solution (drying at 58°C) is ca. $3\ \mu\text{m}$ with its typical square morphology. On the other hand, the size of FAPbBr_3 is dramatically reduced when using the same anti-solvent precipitation in presence of $g\text{-C}_3\text{N}_4$ as seed, this phenomenon was also observed in other FAPbBr_3 -involved nanohybrids, due to the extra nucleation sites [1,18,19]. For the $\text{FAPbBr}_3/\text{C}_3\text{N}_4$ hybrids, the size of $g\text{-C}_3\text{N}_4$ is few tens micrometres and the decorated FAPbBr_3 nanocrystals is few nanometres in size, from which the FAPbBr_3 nanocrystals can hardly be identified using SEM due to the too small size (Figure S2). Thus, the high-resolution transmission electron microscopy (HRTEM) is employed to further investigate the crystal structure and morphology of as-prepared $\text{FAPbBr}_3/\text{C}_3\text{N}_4$ hybrids. The $g\text{-C}_3\text{N}_4$ exhibits a typical plate-like morphology attributing to its graphite structure (Figure 1a,b), for contrast, darker spots of ca. $10\ \text{nm}$ in size are observed on the $g\text{-C}_3\text{N}_4$ after the decoration of FAPbBr_3 nanocrystals (Figure 1c,d), these darker spots are confirmed to be FAPbBr_3 by select area electron diffraction (SAED, Figure 1c), in which the electron diffraction pattern from cubic crystal perovskite is consistent with the previous report [20]. In addition, the elemental formation was confirmed using SEM energy dispersive X-ray spectroscopy (EDX, Figure S3), the elements being detected were consistent with the predominant elements in $g\text{-C}_3\text{N}_4$ and FAPbBr_3 . Besides the morphological variation, no obvious chemical state differences of pristine are revealed by exploiting X-ray photoelectron spectroscopy (XPS) in the nanohybrid materials (Figure S4). As shown in Figure S4b, the XPS spectrum of $g\text{-C}_3\text{N}_4$ clearly records three peaks with different binding energies of 287.2 and $397.6\ \text{eV}$ corresponding to the core level of C $1s$ and N $1s$, respectively. Consistently, the binding energy of Pb $4f$ (Figure S4c) in FAPbBr_3 is 137.4 and $142.3\ \text{eV}$, assigned to Pb $4f_{7/2}$ and Pb $4f_{5/2}$ [21]. The binding energy of Br $3d$ in FAPbBr_3 (Figure S4d) at 67.2 and $68.1\ \text{eV}$, corresponding to Br $3d_{5/2}$ and Br $3d_{3/2}$ [22]. FAPbBr_3 chemically reacts with C-NH_x in C_3N_4 to generate C-N-Br bond due to the sp^2 -hybridised nitrogen in C_3N_4 [23–25]. In this manner of chemical

bonding, the lone pair electrons provided by FAPbBr₃ can neutralise the positive charge effect of hybridisation. The positive shift of binding energy of Br 3d in hybrids (Figure S4d) could support above reasoning. Similarly, it can be inferred that the positive shift of binding energy of Pb in hybrids (Figure S4c) is to balance the electron redistribution in hybrids. In addition, binding energy of Pb 4f and Br 3d presented shift toward greater energy after coupling with g-C₃N₄, this is accompanied by an increased electron density and enhanced electron-donating ability for FAPbBr₃ side. As a result, an internal electric field undergoing electron transfer from FAPbBr₃ to g-C₃N₄ is constructed, and accordingly, holes from g-C₃N₄ to FAPbBr₃.

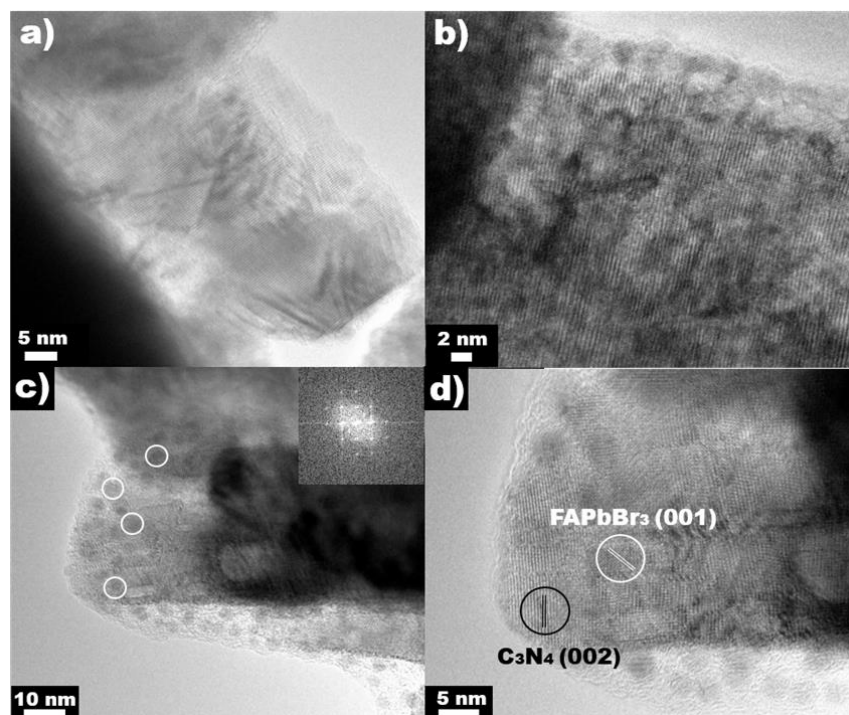


Figure 1. (a) TEM image of the pristine g-C₃N₄ nanoplate; (b) HRTEM image of FAPbBr₃/C₃N₄ hybrids; (c) FAPbBr₃/C₃N₄ hybrids in which the FAPbBr₃ nanocrystals are labelled by white circle with SAED on the right top in this image; (d) the lattice fringes of g-C₃N₄ (002) and FAPbBr₃ (001), respectively.

2.2. Optical Features

The optical properties of g-C₃N₄, FAPbBr₃ and FAPbBr₃/C₃N₄ are characterised by UV-vis diffuse reflectance spectroscopy (DRUVS, Figure 2). Typical absorption edges and band gaps are exhibited for a series of materials: 441 nm (ca. 2.81 eV) for g-C₃N₄ and 560 nm (2.21 eV) for FAPbBr₃, which are consistent with the previous reports.

In comparison to the pristine g-C₃N₄, a substantial enhancement of absorption capability is observed from FAPbBr₃/C₃N₄ hybrids due to the adding of FAPbBr₃, especially in the visible region. In addition, with respect to the pristine FAPbBr₃, the hybrid materials exhibit a slight blue shift of ca. 15 nm, which could be attributed to the crystal size reduction [26]. FAPbBr₃/C₃N₄ hybrid materials with 5, 10, 20 and 30 wt% of FAPbBr₃ are prepared, elevating the weight ratio of FAPbBr₃ in the hybrids leading to an increased visible region absorption.

In addition to the absorption spectrum, the emission of hybrid materials and pristine materials is determined by steady-state photoluminescence (PL) spectra to demonstrate the photophysical benefit of the formation of the hybrid system. Figure 3 presents PL spectra of g-C₃N₄, FAPbBr₃ and FAPbBr₃/C₃N₄ with different weight ratios, in which the pristine g-C₃N₄ and FAPbBr₃ exhibit the typical PL emission peaks centred at ca. 442 and 562 nm, respectively. On the other hand, the FAPbBr₃/C₃N₄ hybrids show obviously quenched PL emission intensity with respect to pristine g-C₃N₄, especially for the one loaded with 20%

perovskite, suggesting that the photoinduced charge recombination rate occurring in the hybrids has been partially inhibited [7].

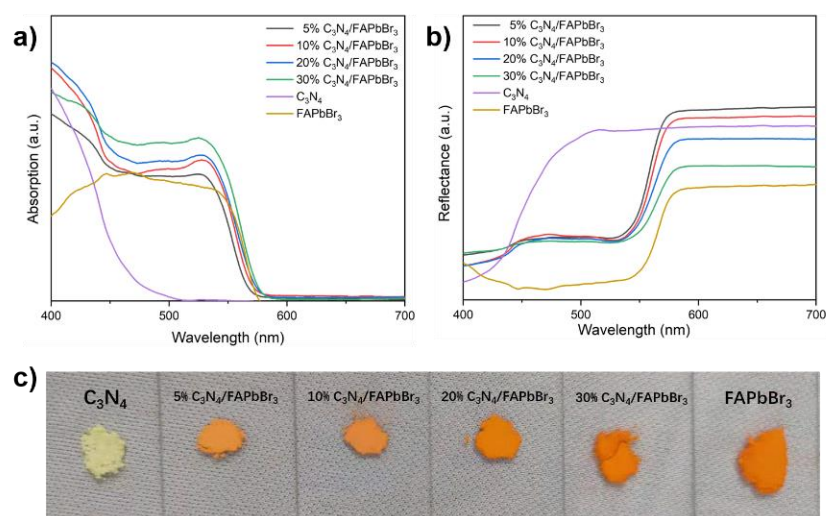


Figure 2. (a) UV-vis absorption spectrum of FAPbBr₃/C₃N₄ hybrids materials with different weight ratio of FAPbBr₃; (b) UV-vis diffuse reflectance spectrum and (c) digital photographs of FAPbBr₃/C₃N₄ hybrids.

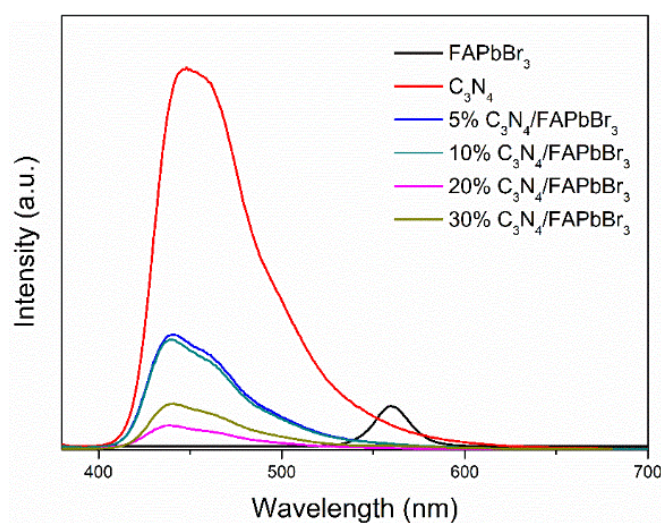


Figure 3. PL spectrum of FAPbBr₃/C₃N₄ hybrids materials with different weight ratio of FAPbBr₃, g-C₃N₄ and FAPbBr₃.

2.3. Photocatalytic Activity

The photocatalytic performances of the whole sample series are evaluated via selective photocatalytic oxidation of benzylic alcohol. Certain amounts (Supporting Information) of samples are put in an apolar solvent (trifluorotoluene) with molecular oxygen injection, and the Xe lamp with AM 1.5 G filter is then applied (100 mW cm⁻²) as a simulated solar illumination. For the photocatalytic activity test, the pristine FAPbBr₃ (10 mg) and g-C₃N₄ (10 mg) are exploited as controls, giving the conversion rate of ca. 14.6% and 1.8% after an illuminated duration of 4 h (in 1.5 mL trifluorotoluene containing 0.1 mmol benzyl alcohol, saturated with oxygen), respectively (the photocatalytic conversion rate of samples and control groups are summarised in Table S1 under above conditions). As it is shown in Figure 4a for photoactivity results, the hybrids exhibit a substantial improvement compared to the pristine materials. About half-fold activity enhancement is obtained

by adding 5 wt% of FAPbBr₃, in comparison to pure FAPbBr₃. The best performance of ca. 46.6% conversion rate (4 h illumination) is achieved from the hybrid with 20 wt% of FAPbBr₃, which is approximately three-fold enhancement over pristine FAPbBr₃ control group. The conversion rate of 10 mg 20 wt% FAPbBr₃/C₃N₄ could be further enhanced to 69.5% with 8 h illumination (Figure 4b) at room temperature, which can be compared to that of FAPbBr₃/TiO₂ (10 mg, 8 h illumination at room temperature, 63% conversion rate, 99% selectivity) [19] and mpg-C₃N₄ (50 mg, 3 h illumination at 100 °C, 70% conversion rate, 68% selectivity) [27]. In addition, further increasing the FAPbBr₃ weight ratio over 20 wt% will lead to a reduction of conversion rate. This could be due to two reasons: (1) The overloaded FAPbBr₃ in hybrid reduces the g-C₃N₄ surface area available exposed to the reagent in apolar solvent; (2) the increased amount of FAPbBr₃ nanocrystals indicates more interfaces and recombination centres, as it was observed in PL spectra (Figure 3). Based on both factors, excessive loading of FAPbBr₃ will not be necessary for pursuing further optimisation of photocatalytic performance. Furthermore, adjusting the weight ratio between FAPbBr₃ and g-C₃N₄ will not compromise the high selectivity (over 98% across all hybrids) for benzylic alcohol oxidation.

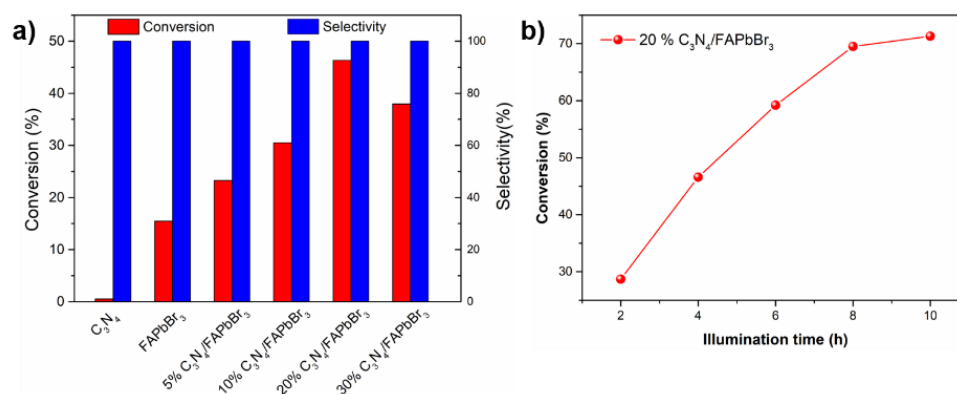


Figure 4. (a) Photocatalytic oxidation of benzylic alcohol to benzaldehyde over pristine FAPbBr₃/C₃N₄ of different weight ratios, noted that the pure FAPbBr₃ is of ca. 3 μm; (b) photocatalytic oxidation of benzylic alcohol using 20% FAPbBr₃/C₃N₄ under different illumination durations, the data is averaged from 3 individual tests. Reaction conditions: photocatalyst (10 mg) and 0.1 mmol reactant, in trifluorotoluene (1.5 mL) saturated with oxygen before experiments, irradiated by AM 1.5G (ca. 100 mW cm⁻²) for 4 h each cycle, under room temperature.

To further realise the photocatalytic process, electron spin resonance (ESR) spectroscopy is exploited to confirm the photo-induced reactive oxygen species, under simulated solar illumination. 5,5-Dimethyl-1-Pyrroline N-oxide (DMPO) is employed as a trapping agent. Negligible signals from DMPO••O₂⁻ is observed in absence of illumination for hybrids (Figure 5). When the simulated illumination is applied, however, significantly increased ESR signals generated from DMPO••O₂⁻ are recorded, suggesting that the reduction of O₂ to •O₂⁻ is triggered by photo-induced electrons from hybrids. Besides the •O₂⁻ signals, an additional ESR signal raised by nitroxide radical is observed, this could be attributed to the photo-induced cleavage of ring opening of DMPO••O₂⁻ [28]. The photocatalytic process of benzyl alcohol oxidation using OHIPs and hybrids is illustrated below in Figure 6. As demonstrated in previous reports [29,30], the generation of h⁺ and •O₂⁻ would lead to the formation of benzaldehyde. Another possible product form benzyl alcohol oxidation is benzoic acid, which would be formed in presence of •OOH radicals. While in this work, no •OOH radicals are monitored, resulting in the high selectivity of samples.

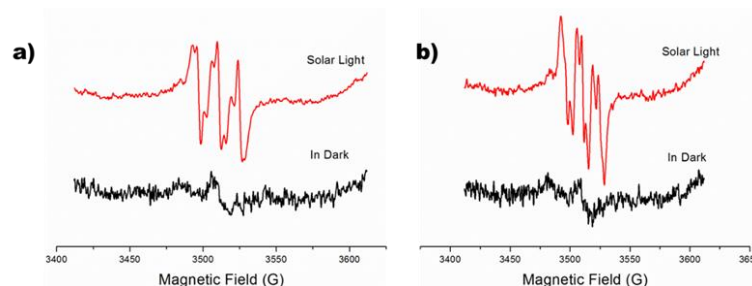


Figure 5. ESR spectra of (a) FAPbBr₃ and (b) 20% FAPbBr₃/C₃N₄ hybrids.

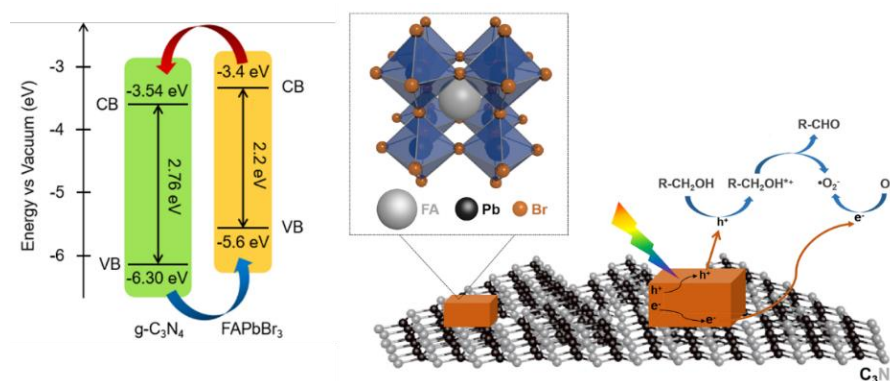


Figure 6. Schematic illustration of photo-catalytic reaction occurring on FAPbBr₃/C₃N₄ hybrids.

2.4. Stability Investigation

The aim of the photostability tests is to evaluate the potential influence of g-C₃N₄ on the FAPbBr₃/C₃N₄ hybrids, since it may lead to different stability behaviour in comparison to that of typical FAPbBr₃/metal oxide photocatalyst. The photostability of samples is initially demonstrated by repeating the photocatalytic cycles (4 h under illumination) with refilled reactant (benzylic alcohol) for six times. In terms of the pristine FAPbBr₃ sample, the photoactivity loss is ca. 7.2% relative to its conversion rate in the first cycle, with a steady decreasing rate in the subsequent five cycles. In contrast, the FAPbBr₃/C₃N₄ hybrids with different weight ratios presented similar photostability trend (Figure S5). For instance, the photoactivity loss of 20% FAPbBr₃/C₃N₄ hybrids is ca. 16.9% after the first reaction cycle, and then the photoactivity remains stable from two to six reaction cycles (Figure 7a,b). The reduced photoactivity after reaction cycles in OIHPs-involved hybrids is a common phenomenon, it was typically concluded as that the product (benzaldehyde) offers higher polarity than the reactant (benzylic alcohol), and thus the illumination accelerates the dissolution of FAPbBr₃ [19], which would partially explain the photoactivity decrease in both pure FAPbBr₃ and hybrids. However, in comparison to the pristine FAPbBr₃, FAPbBr₃/C₃N₄ exhibits different trends of photostability (Figure 7a,b), suggesting that other factors should be considered in these photoactivated reactions.

Thus, in order to further realise the stability behaviours of FAPbBr₃/C₃N₄, a comparison is made between FAPbBr₃/C₃N₄ and FAPbBr₃/WO₃ hybrids (see Figures S6–S8 in supporting Information for details of the as-prepared FAPbBr₃/WO₃). WO₃ has a similar band gap energy with that of C₃N₄ (ca. 2.81 eV). Besides, both of WO₃ and C₃N₄ present plate-like morphology when prepared through common methods. Different from the FAPbBr₃/C₃N₄, FAPbBr₃/WO₃ exhibits a steady photoactivity decreasing along with the six cycles, which is consistent with the behaviours of pristine FAPbBr₃ and other typical OIHPs/metal oxides hybrids [30–32]. These results suggest that g-C₃N₄ should possibly be responsible for the FAPbBr₃/C₃N₄ photostability behaviour instead of the construction of hybrids. Next, long-pass filter (420 nm, 450 nm and 500 nm) is applied on samples (FAPbBr₃/C₃N₄, WO₃/FAPbBr₃ and FAPbBr₃) to demonstrate the dependence of incident wavelength of light. When applying the long-pass filter (420 nm), the photostability of the

three samples present photostability of similar trends, comparing to each of that under white light illumination, respectively. While relative to that under 420 nm long-pass filter, the FAPbBr₃/C₃N₄ sample performs different trend of photostability (no dramatic conversion rate decreasing was found after first cycle) after employing the 450 nm (Figure 7c,d) or 500 nm long-pass filter (summarised in Table S2, supporting information). After 1 reaction cycles under illumination without filters, the conversion rate of FAPbBr₃, FAPbBr₃/WO₃ and FAPbBr₃/C₃N₄ decreased 7.2%, 7% and 16.9%, respectively. Then, FAPbBr₃/C₃N₄ (20 wt%) exhibits outstanding photostability during two to six cycles, only less than 1% photoactivity loss, which can be compared to FAPbBr₃ (19.2%) and FAPbBr₃/WO₃ (19%).

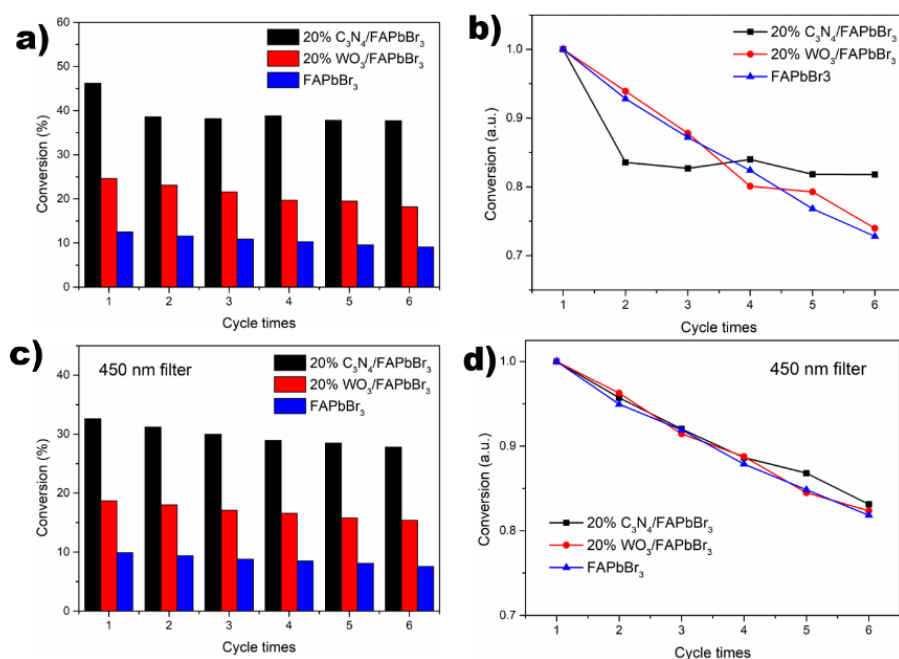


Figure 7. (a) The conversion rate of 20% FAPbBr₃/C₃N₄ and control groups under Xe lamp illumination for 6 cycles; (b) the conversion rate relative to the first cycle under Xe lamp illumination; (c,d) conversion rate for six cycles and conversion rate relative to the first cycle when applying a 450 nm long-pass filter, respectively. Reaction conditions: photocatalyst (10 mg) and 0.1 mmol reactant, trifluorotoluene (1.5 mL) saturated with oxygen before experiments, irradiated by AM 1.5 G (ca. 100 mW cm⁻²) for 4 h each cycle, under room temperature.

As it was known that g-C₃N₄ and FAPbBr₃ would construct a typical type-II band structure, in which the holes migrate from the valence band (VB) of g-C₃N₄ to the VB of FAPbBr₃ for benzylic alcohol oxidation reaction. During the preparation of samples, it is unavoidable that pristine g-C₃N₄ and FAPbBr₃ would be in presence in the as-prepared FAPbBr₃/C₃N₄ samples. The pristine g-C₃N₄ typically exhibits a higher oxidation potential than this type-II hybrid. When the energy of incident photons is greater than the band gap of pristine g-C₃N₄ (2.81 eV, 441 nm), the higher oxidation potential of g-C₃N₄ (with respect to FAPbBr₃/C₃N₄) allows the oxidizing of N-H moieties into imines [33], which would partially consume the FA⁺(HC(NH₂)₂)⁺ and Br⁻ moieties in FAPbBr₃, especially those on the surface of FAPbBr₃ nanocrystals, thus resulting in decreasing of conversion rate after the first photocatalytic cycle. However, the oxidised N-H moieties typically present good tolerance to the typical polar solvent [14], therefore leading to the optimised photostability during the two to six cycles (Figure 7b). As a result, although the photoactivity FAPbBr₃/C₃N₄ hybrids reduced 16.9% in the first cycle, only less than 1% conversion rate loss is recorded in the subsequent five cycles.

Furthermore, we compared the SEM images and XRD patterns of samples before and after the photocatalytic reactions. It should be noted that we focus on the possible morphology or crystal structure changes of FAPbBr₃, since the g-C₃N₄ is extremely chem-

ically stable [34]. FAPbBr₃ of few tens micrometre scale in size is prepared (by slowing the crystallisation process at lower temperature) for convenient morphology evaluation, because the nanocrystals are too small to be monitored using SEM. Before the photocatalytic reactions, the FAPbBr₃ crystals present the typical cubic-like morphology with smooth surface (Figure 8a). The surface of pristine FAPbBr₃ caved in (Figure 8b) after one photocatalytic reaction cycle, which could be due to the FA⁺ dissolution. On the other hand, interestingly, we observed stripes and intersected nanorods (red square frame in Figure 8c) on the surface of FAPbBr₃ crystals when g-C₃N₄ is present. We believe this is highly possible to be the surface passivation attributing to the presence of g-C₃N₄ and thus preventing the photoactivity from dropping in the stability tests. In addition, there are no XRD patterns changes detected for these samples before and after photocatalysis, suggesting the samples mainly remain in their crystal structures.

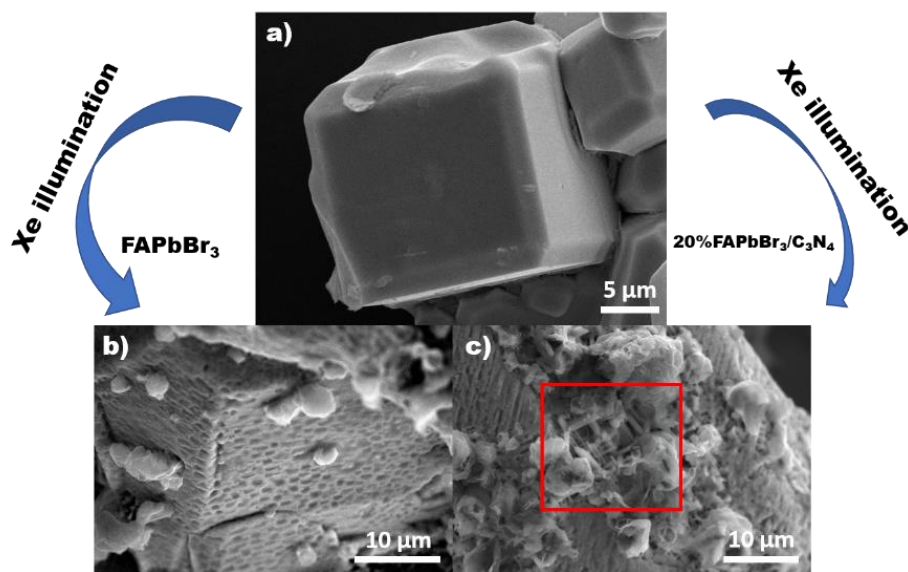


Figure 8. SEM image of (a) FAPbBr₃ crystals prepared at 25 °C using anti-solvent method; (b) pristine FAPbBr₃ crystals after the photocatalytic oxidation of benzylic alcohol; (c) FAPbBr₃ crystals after the photocatalytic oxidation of benzylic alcohol when g-C₃N₄ is present.

3. Conclusions

In summary, a hybrid photocatalyst formed by g-C₃N₄ and FAPbBr₃ is developed for highly stable and efficient photocatalytic oxidation of benzylic alcohol into aldehydes, which performs a three-fold enhancement in photocatalytic efficiency compared with pristine FAPbBr₃. In addition, the uncommon photostability behaviour of FAPbBr₃/C₃N₄ hybrids under white light illumination is realised by detailed comparing with metal oxide/FAPbBr₃ hybrids and pristine FAPbBr₃. As a result, although the coupled g-C₃N₄ would increase the photoactivity loss of hybrids in the original photocatalytic reactions, the photostability is dramatically enhanced in the subsequent reactions. We believe this would supply insights for OHIPs-involved optoelectronic applications toward the stability issues.

Supplementary Materials: The following are available online at <https://www.mdpi.com/article/10.3390/catal11040505/s1>, Figure S1. PXRD of FAPbBr₃/C₃N₄ hybrids, where A = diffraction pattern from (110) of g-C₃N₄ (JCPDS# 87-1526), the rest of the diffraction patterns are consistent with FAPbBr₃ from a previous report. Figure S2. SEM images of (a) prinstin FAPbBr₃ crystals synthesis through anti-solvent method and their size distribution; (b)–(d) FAPbBr₃/C₃N₄ hybrids materials. Figure S3. Selected area EDX analysis of the as-prepared FAPbBr₃/C₃N₄ samples, with detailed elemental distribution. Figure S4. XPS spectrum of a C₃N₄/FAPbBr₃ hybrids materials; (b) prinstine g-C₃N₄; (c–f) bind energy of Pb 4f orbitals, Br 3d orbitals, C 1s orbitals and N 1s orbitals, respectively. Figure S5. The photoactivity of C₃N₄/FAPbBr₃ hybrids materials with respect to the photoactivity in the first cycle of each. The reaction conditions are consistent with other tests.

Figure S6. HRTEM of (a) WO₃ nanoplate and (b) WO₃/FAPbBr₃ hybrids materials. Figure S7. TEM-HAADF image and according elemental mapping of WO₃/FAPbBr₃ hybrids materials. Figure S8. PXRD of WO₃/FAPbBr₃ hybrids with different FAPbBr₃ weight ratios, in which # = FAPbBr₃ and * = WO₃ (JCPDS# 43-1035), respectively. Table S1. Photocatalytic oxidation of benzylic alcohol using a series of samples. Table S2. Photocatalytic oxidation of benzylic alcohol using a series of samples with long-pass filter (420 nm, 450 nm and 500 nm).

Author Contributions: Conceptualization, M.Z., W.W. and F.G.; Fomal analysis, M.Z. and W.W.; Writing—original draft, M.Z. and W.W.; Writing—review and editing, M.Z., W.W. and F.G.; Funding acquisition, M.Z., F.G. and D.L. All authors have read and agreed to the published version of the manuscript.

Funding: This research was funded by the Guangdong Basic and Applied Basic Research Foundation (Grant Nos. 2020B1515020032, 2020B1515120022), the National Natural Science Foundation of China (Grant Nos. 62074060, 52002135), the Guangdong Science and Technology Plan (Grant No. 2019B040403003), the Pearl River Talent Recruitment Program (Grant No. 11804058), the Natural Science Foundation of Guangdong Province (Grant No. 2018A0303130199), the Program for Guangdong Introducing Innovative and Entrepreneurial Teams (2016ZT06C412) and the Scientific and Technological Plan of Guangdong Province, China (No. 2019B090905005).

Conflicts of Interest: The authors declare no conflict of interest.

References

1. Zhao, Y.; Zhu, K. ChemInform Abstract: Organic-Inorganic Hybrid Lead Halide Perovskites for Optoelectronic and Electronic Applications. *Chem. Soc. Rev.* **2016**, *47*, 655–689. [[CrossRef](#)] [[PubMed](#)]
2. Kazim, S.; Nazeeruddin, M.K.; Gratzel, M.; Ahmad, S. Perovskite as light harvester: A game changer in photovoltaics. *Angew. Chem.* **2014**, *53*, 2812–2824. [[CrossRef](#)] [[PubMed](#)]
3. Wang, X.; Maeda, K.; Thomas, A.; Takanabe, K.; Xin, G.; Carlsson, J.M.; Domen, K.; Antonietti, M. A metal-free polymeric photocatalyst for hydrogen production from water under visible light. *Nat. Mater.* **2009**, *8*, 76–80. [[CrossRef](#)] [[PubMed](#)]
4. Zhou, M.; Hou, Z.; Zhang, L.; Liu, Y.; Gao, Q.; Chen, X. n/n junctioned g-C₃N₄ for enhanced photocatalytic H₂ generation. *Sustain. Energy Fuels* **2017**, *1*, 317–323. [[CrossRef](#)]
5. Kang, Y.; Yang, Y.; Yin, L.C.; Kang, X.; Liu, G.; Cheng, H.M. An Amorphous Carbon Nitride Photocatalyst with Greatly Extended Visible-Light-Responsive Range for Photocatalytic Hydrogen Generation. *Adv. Mater.* **2015**, *27*, 4572–4577. [[CrossRef](#)]
6. Zhou, Z.; Zhang, Y.; Shen, Y.; Liu, S.; Zhang, Y. Molecular engineering of polymeric carbon nitride: Advancing applications from photocatalysis to biosensing and more. *Chem. Soc. Rev.* **2018**, *47*, 2298–2321. [[CrossRef](#)]
7. Wang, Y.; Zhen, W.; Zeng, Y.; Wan, S.; Guo, H.; Zhang, S.; Zhong, Q. In situ self-assembly of zirconium metal–organic frameworks onto ultrathin carbon nitride for enhanced visible light-driven conversion of CO₂ to CO. *J. Mater. Chem. A* **2020**, *8*, 6034–6040. [[CrossRef](#)]
8. Yang, X.; Tang, H.; Xu, J.; Antonietti, M.; Shalom, M. Silver phosphate/graphitic carbon nitride as an efficient photocatalytic tandem system for oxygen evolution. *ChemSusChem* **2015**, *8*, 1350–1358. [[CrossRef](#)]
9. Zhang, G.; Huang, C.; Wang, X. Dispersing molecular cobalt in graphitic carbon nitride frameworks for photocatalytic water oxidation. *Small* **2015**, *11*, 1215–1221. [[CrossRef](#)]
10. Ming, J.; Liu, A.; Zhao, J.; Zhang, P.; Huang, H.; Lin, H.; Xu, Z.; Zhang, X.; Wang, X.; Hofkens, J.; et al. Hot pi-Electron Tunneling of Metal-Insulator-COF Nanostructures for Efficient Hydrogen Production. *Angew. Chem.* **2019**, *58*, 18290–18294. [[CrossRef](#)] [[PubMed](#)]
11. Pan, Z.; Zheng, Y.; Guo, F.; Niu, P.; Wang, X. Decorating CoP and Pt Nanoparticles on Graphitic Carbon Nitride Nanosheets to Promote Overall Water Splitting by Conjugated Polymers. *ChemSusChem* **2017**, *10*, 87–90. [[CrossRef](#)] [[PubMed](#)]
12. Park, S.; Chang, W.J.; Lee, C.W.; Park, S.; Ahn, H.-Y.; Nam, K.T. Photocatalytic hydrogen generation from hydriodic acid using methylammonium lead iodide in dynamic equilibrium with aqueous solution. *Nat. Energy* **2016**, *2*, 16185. [[CrossRef](#)]
13. Pu, Y.-C.; Fan, H.-C.; Liu, T.-W.; Chen, J.-W. Methylamine lead bromide perovskite/protonated graphitic carbon nitride nanocomposites: Interfacial charge carrier dynamics and photocatalysis. *J. Mater. Chem. A* **2017**, *5*, 25438–25449. [[CrossRef](#)]
14. Luo, B.; Pu, Y.-C.; Lindley, S.A.; Yang, Y.; Lu, L.; Li, Y.; Li, X.; Zhang, J.Z. Organolead Halide Perovskite Nanocrystals: Branched Capping Ligands Control Crystal Size and Stability. *Angew. Chem.* **2016**, *128*, 9010–9014. [[CrossRef](#)]
15. Sheldon, R.A.; Arends, I.W.C.E.; Dijkstra, A. New developments in catalytic alcohol oxidations for fine chemicals synthesis. *Catal. Today* **2000**, *57*, 157–166. [[CrossRef](#)]
16. Eperon, G.E.; Stranks, S.D.; Menelaou, C.; Johnston, M.B.; Herz, L.M.; Snaith, H.J. Formamidinium lead trihalide: A broadly tunable perovskite for efficient planar heterojunction solar cells. *Energy Environ. Sci.* **2014**, *7*, 982. [[CrossRef](#)]
17. Wang, J.; Song, C.; He, Z.; Mai, C.; Xie, G.; Mu, L.; Cun, Y.; Li, J.; Wang, J.; Peng, J. All-Solution-Processed Pure Formamidinium-Based Perovskite Light-Emitting Diodes. *Adv. Mater.* **2018**, *30*, e1804137. [[CrossRef](#)]

18. Zheng, K.; Židek, K.; Abdellah, M.; Messing, M.E.; Al-Marri, M.J.; Pullerits, T. Trap States and Their Dynamics in Organometal Halide Perovskite Nanoparticles and Bulk Crystals. *J. Phys. Chem. C* **2016**, *120*, 3077–3084. [[CrossRef](#)]
19. Huang, H.; Yuan, H.; Janssen, K.P.F.; Solís-Fernández, G.; Wang, Y.; Tan, C.Y.X.; Jonckheere, D.; Debroye, E.; Long, J.; Hendrix, J.; et al. Efficient and Selective Photocatalytic Oxidation of Benzylic Alcohols with Hybrid Organic–Inorganic Perovskite Materials. *ACS Energy Lett.* **2018**, *3*, 755–759. [[CrossRef](#)]
20. Fu, Y.; Zhu, H.; Schrader, A.W.; Liang, D.; Ding, Q.; Joshi, P.; Hwang, L.; Zhu, X.Y.; Jin, S. Nanowire Lasers of Formamidinium Lead Halide Perovskites and Their Stabilized Alloys with Improved Stability. *Nano Lett.* **2016**, *16*, 1000–1008. [[CrossRef](#)]
21. Deepa, M.; Salado, M.; Calio, L.; Kazim, S.; Shivaprasad, S.M.; Ahmad, S. Cesium power: Low Cs⁺ levels impart stability to perovskite solar cells. *Phys. Chem. Chem. Phys.* **2017**, *19*, 4069–4077. [[CrossRef](#)] [[PubMed](#)]
22. Leng, M.; Chen, Z.; Yang, Y.; Li, Z.; Zeng, K.; Li, K.; Niu, G.; He, Y.; Zhou, Q.; Tang, J. Lead-Free, Blue Emitting Bismuth Halide Perovskite Quantum Dots. *Angew. Chem.* **2016**, *55*, 15012–15016. [[CrossRef](#)] [[PubMed](#)]
23. Liu, G.; Zhao, G.; Zhou, W.; Liu, Y.; Pang, H.; Zhang, H.; Hao, D.; Meng, X.; Li, P.; Kako, T.; et al. In Situ Bond Modulation of Graphitic Carbon Nitride to Construct p-n Homojunctions for Enhanced Photocatalytic Hydrogen Production. *Adv. Funct. Mater.* **2016**, *26*, 6822–6829. [[CrossRef](#)]
24. Yang, P.; Ou, H.; Fang, Y.; Wang, X. A Facile Steam Reforming Strategy to Delaminate Layered Carbon Nitride Semiconductors for Photoredox Catalysis. *Angew. Chem.* **2017**, *129*, 4050–4054. [[CrossRef](#)]
25. Shi, L.; Chang, K.; Zhang, H.; Hai, X.; Yang, L.; Wang, T.; Ye, J. Drastic Enhancement of Photocatalytic Activities over Phosphoric Acid Protonated Porous g-C₃N₄ Nanosheets under Visible Light. *Small* **2016**, *12*, 4431–4439. [[CrossRef](#)]
26. Wu, Y.; Wang, P.; Zhu, X.; Zhang, Q.; Wang, Z.; Liu, Y.; Zou, G.; Dai, Y.; Whangbo, M.H.; Huang, B. Composite of CH₃NH₃PbI₃ with Reduced Graphene Oxide as a Highly Efficient and Stable Visible-Light Photocatalyst for Hydrogen Evolution in Aqueous HI Solution. *Adv. Mater.* **2018**, *30*, 1704342. [[CrossRef](#)]
27. Su, F.; Mathew, S.C.; Lipner, G.; Fu, X.; Antonietti, M.; Blechert, S.; Wang, X. mpg-C₃N₄-Catalyzed selective oxidation of alcohols using O₂ and visible light. *J. Am. Chem. Soc.* **2010**, *132*, 16299–16301. [[CrossRef](#)]
28. Diaz-Urbe, C.E.; Daza, M.C.; Martínez, F.; Páez-Mozo, E.A.; Guedes, C.L.B.; Di Mauro, E. Visible light superoxide radical anion generation by tetra(4-carboxyphenyl)porphyrin/TiO₂: EPR characterization. *J. Photochem. Photobiol. A Chem.* **2010**, *215*, 172–178. [[CrossRef](#)]
29. Huang, H.; Zhao, J.; Du, Y.; Zhou, C.; Zhang, M.; Wang, Z.; Weng, Y.; Long, J.; Hofkens, J.; Steele, J.A.; et al. Direct Z-Scheme Heterojunction of Semicoherent FAPbBr₃/Bi₂WO₆ Interface for Photoredox Reaction with Large Driving Force. *ACS Nano* **2020**, *14*, 16689–16697. [[CrossRef](#)]
30. Huang, H.; Yuan, H.; Zhao, J.; Solís-Fernández, G.; Zhou, C.; Seo, J.W.; Hendrix, J.; Debroye, E.; Steele, J.A.; Hofkens, J.; et al. C(sp³)-H Bond Activation by Perovskite Solar Photocatalyst Cell. *ACS Energy Lett.* **2019**, *4*, 203–208. [[CrossRef](#)]
31. Mali, S.S.; Patil, J.V.; Kim, H.; Hong, C.K. Synthesis of SnO₂ nanofibers and nanobelts electron transporting layer for efficient perovskite solar cells. *Nanoscale* **2018**, *10*, 8275–8284. [[CrossRef](#)] [[PubMed](#)]
32. Subbiah, A.S.; Agarwal, S.; Mahuli, N.; Nair, P.; van Hest, M.; Sarkar, S.K. Stable p-i-n FAPbBr₃ Devices with Improved Efficiency Using Sputtered ZnO as Electron Transport Layer. *Adv. Mater. Interface* **2017**, *4*, 1601143. [[CrossRef](#)]
33. Su, F.; Mathew, S.C.; Mohlmann, L.; Antonietti, M.; Wang, X.; Blechert, S. Aerobic oxidative coupling of amines by carbon nitride photocatalysis with visible light. *Angew. Chem.* **2011**, *50*, 657–660. [[CrossRef](#)]
34. Yang, T.; Huang, Y.; Yang, L.; Li, X.; Wang, X.; Zhang, G.; Luo, Y.; Jiang, J. Protecting Single Atom Catalysts with Graphene/Carbon-Nitride “Chainmail”. *J. Phys. Chem. Lett.* **2019**, *10*, 3129–3133. [[CrossRef](#)] [[PubMed](#)]